Quirk *et al. Fluids and Barriers of the CNS* (2026) 23:41
https://doi.org/10.1186/s12987-026-00782-w

Fluids and Barriers of the CNS

RESEARCH Open Access

Quantifying cerebrospinal fluid flow in pial perivascular spaces of rats

Keelin Quirk[1†], Antonio Ladrón-de-Guevara[2,3†], Aditya Raghunandan[4,5], Humberto Mestre[6], Maiken Nedergaard[3,7] and Douglas H. Kelley[1*]

Abstract

The circulation of cerebrospinal fluid (CSF) through perivascular spaces (PVSs) has been proposed to play a role in clearing waste from the brain. While several studies have quantified such flow in mice, no in vivo studies with high spatial and temporal resolution have been performed on other species. Here, we imaged pial PVSs of rat brains and the CSF flows they carry, using techniques previously employed with mice. Using vessel pulsatility measurement and automated particle tracking, we quantified and analyzed in vivo CSF velocity profiles, artery wall motion, and PVS resistances in rats, comparing our findings to mice. Both species exhibit net CSF flows in the same direction as blood flow, and CSF pulsations are substantially synchronized with the heartbeat. We found that rats have larger, lower-resistance PVSs, resulting in much larger CSF volume flow rates in rats than in mice. We also found that the choice of anesthetic can significantly affect vasomotion and corresponding CSF pulsations in rats, with ketamine-dexmedetomidine producing a more stable response than ketamine-xylazine. Our results can be used in models of flow through rat PVSs, and as experiments are performed on additional species, can aid in projecting results across scales from animal models to human CSF flows.

Introduction

The movement of cerebrospinal fluid (CSF) within perivascular spaces (PVSs), which are annular channels enveloping the brain's vasculature, appears to aid in eliminating metabolic waste from brain tissue [1–3]. Inadequate removal of waste products, including harmful protein species, has been associated with neurological and age-related disorders [4–7]. The link between human brain disorders and glymphatic dysfunction has sparked significant interest in comprehending the characteristics of PVS geometries and CSF flows, along with the mechanisms that propel these flows [8].

Much of our understanding of how CSF flows through PVSs is the result of in vivo experiments imaging fluid flows in pial PVSs of mice. Considerable research has been done to investigate the movement of CSF within the pial PVS of mice during states of sleep [3, 9] and anesthesia [10–13]. Additionally, the geometries and resistances

---

[†] Keelin Quirk and Antonio Ladrón-de-Guevara contributed equally to this work.

*Correspondence:
Douglas H. Kelley
d.h.kelley@rochester.edu
[1] Department of Mechanical Engineering, University of Rochester, Rochester, NY, USA
[2] Department of Biomedical Engineering, University of Rochester, Rochester, NY, USA
[3] Center for Translational Neuromedicine, University of Rochester Medical Center, Rochester, NY, USA
[4] Department of Mechanical Engineering, University of Michigan-Dearborn, Dearborn, MI, USA
[5] Weil Institute for Critical Care Research and Innovation, University of Michigan, Ann Arbor, MI 48109, USA
[6] Department of Neurology, Massachusetts General Brigham, Harvard Medical School, Boston, MA, USA
[7] Center for Translational Neuromedicine, University of Copenhagen, Copenhagen N 2200, Denmark

of pial PVSs have been carefully quantified to allow more accurate models of CSF flow [14–16]. In perivascular spaces, solutes have been found to be transported primarily by advection, based on calculations of the Péclet number [12, 17], and the flow is correlated with arterial pulsations [12, 13, 18].

Exploring PVS geometries and CSF flow rates in rats, not just mice, is important for at least three reasons. First, mathematical models of the CSF flows in the brain depend on species-specific measurements of channel geometries and mean speeds, and thus consider just one species each. Usually, such models simulate mice [19–21] as their glymphatic channels are most precisely characterized [14, 22]. The high-fidelity models of individual PVSs and low-fidelity brain-wide models previously developed to study mice both require high spatial and temporal resolution measurements of CSF velocities along with three-dimensional characterization of PVS cross-sectional geometry [10]. In rats, most studies have used dynamic contrast–enhanced MRI with kinetic modeling to characterize macroscopic CSF transport, yielding model-derived parameters such as infusion and clearance rates [23–25]. However, the relatively low spatial and temporal resolution of these methods prevents resolution of CSF flow within individual PVSs. To date, direct measurements of CSF dynamics in pial PVSs of live rats have not been performed, so key aspects of rat glymphatic transport remain uncharacterized. Second, relatively little is known about the extent to which glymphatic function is conserved across species. Only a handful of species have been used in glymphatics studies at all: mice, rats, pigs, humans, alligators [26], and recently rabbits [27]. In all species other than mice, previous studies generally lack sufficient quantitative measurements for cross-species comparison, leaving much unknown about the evolution of the glymphatic system [28]. Influx and efflux routes, pumping mechanisms, clearance rates, and glymphatic dependence on brain state are still being elucidated and may well vary across species [29, 30]. Given the likely implications of glymphatic function for human health [4, 31–33], expanding research beyond mice is crucial to improve translation to the clinic and quicker improvement of human outcomes. Finally, understanding how glymphatic function, and specifically fluid and solute transport properties, scale across species would increase the power and flexibility of mathematical models. For example, well-characterized properties of rodent glymphatic systems might be scaled to make accurate predictions of human glymphatic function, despite the fact that many characteristics of the human glymphatic system cannot be measured directly in patients [34].

Rats are physiologically similar to mice, but have larger brains surrounded by a greater volume of CSF. While the technique used for quantifying CSF production can alter the measurement considerably [35], indirect perfusion measurements indicate that young mice produce approximately 0.325 μL/min of CSF [36]. Mice have a total CSF volume of 35 μ L of CSF, implying a turnover time of approximately 1.8 hours [37]. In 3 month old rats, CSF turnover has been measured as approximately 11 times per day, or once every 2.2 hours [38]. From these measurements, it can be calculated that rats produce CSF at a volume flow rate approximately 3.5 times greater, whereas their brain volume is 4.5 times larger [39, 40]. Previously, electron microscopy images of fixed tissue from the rat thalamus identified the existence of perivascular spaces around both arteries and veins [41]. Using tissue that was frozen and then fixed with a phosphate buffer, the width of rat PVSs surrounding arteries was found to be approximately 0.5–1 μ m [42]. However, the fixation process is known to shrink PVSs [12], and such images are not representative of the width of the PVS of a live animal. Moreover, rats possess small arachnoid granulations that provide an additional pathway for CSF efflux, a feature that is largely absent in mice [43, 44]. In humans, arachnoid granulations are thought to be a major route for CSF drainage, making rats a potentially more suitable model for studying CSF outflows [45, 46]. As fluid mass in the brain is conserved, species-specific differences in CSF outflows could also influence measured CSF flow rates in any fluid channels, including pial PVSs.

Despite these differences, MRI and ex vivo techniques indicate that there are substantial similarities in the brain-wide flow and solute transport of mice and rats. Previous experiments indicate that rats do have a brain-wide directional (net) flow of CSF to lymphatic vessels [47]. Perivascular efflux routes have been shown to develop during the first few days of a rat's life, allowing efficient solute clearance [48]. Much like in mice, perivascular solute transport in rats is expected to be dominated by advection [49]. Additionally, anesthesia has usually been seen to enhance glymphatic function in both species, compared to wakefulness [2, 3], though one recent mouse study concluded otherwise [11]. Rats and mice also have similar glymphatic responses to both chronic and acute health challenges. MRI evidence suggests brain-wide drainage is impaired in hypertensive rats [25], while in vivo experiments have similarly observed decreased flow rates in hypertensive mice [12]. Glymphatic function in rats is impaired after traumatic brain injury [50], and similar glymphatic dysfunction is seen in mice [51]. Lastly, glymphatic function is impaired after stroke in both rats [52] and mice [53]. Thus, rats are an interesting subject for in vivo, high-fidelity measurements of CSF flow in pial PVSs, as have previously been made in mice.

In this study, we performed two-photon imaging of the pial PVSs of surface branches of the middle cerebral artery (MCA) of anesthetized young Sprague-Dawley rats, using imaging and analysis procedures previously validated in mice. [13, 15, 54]. Our first aim was to measure pial PVS geometry and CSF flows within PVSs in rats. Our second aim was to compare two common model species, rats and mice, under their commonly recommended anesthetic regimens, by relating our measurements to previously published results for mice [12]. Solute transport via CSF is known to be influenced by anesthetic treatment [55, 56]. However, the two anesthetics used for comparison, xylazine in mice and dexmedetomidine in rats, are both $\alpha2$ adrenergic antagonists that induce a comparable slow-wave-dominant state [57]. Thus, the resulting physiological brain state was equivalent across species, supporting the conceptual comparison of CSF dynamics. We specifically compared the CSF motion, artery pulsation, and PVS size and hydraulic resistance of anesthetized rats and mice.

Materials and methods

Animals and anesthesia

All experimental procedures and imaging protocols used in rats were identical to those previously established and validated in mice. The only minor species-specific adjustments were changes to the length of surgery and recommended anesthetic doses, as required to accommodate anatomical size differences. Experiments were performed according to guidelines of the United States National Institutes of Health, and protocols were approved by the University of Rochester Committee on Animal Resource (UCAR) (Protocol 2011–023). Sprague Dawley rats obtained from Charles River were used (Crl:CD(SD); 8–11 weeks of age; body weight: 250–400 g). Rats were housed in individually ventilated plastic cages in temperature- and light-controlled room with ad libitum access to water and food. For anesthesia, animals were induced with 2–3% isoflurane in oxygen using an induction chamber. This was followed by either an intraperitoneal injection of ketamine/xylazine (100/10 mg/kg) if the rat was anesthetized with KX, or a subcutaneous injection of dexmedetomidine (0.2 mg/kg) if the rat was anesthetized with KD [56]. After exclusions, images from four rats under each anesthetic condition were analyzed in this study. For post-operative analgesia, rats received subcutaneous injections of carprofen (5 mg/kg) and buprenorphine (0.05 mg/kg) at the beginning of surgery. The animals were allowed to breathe spontaneously. Heart and respiratory rate were noninvasively monitored using a small animal physiological monitoring system (Harvard Apparatus) to assure adequate vital signs and temperature during the surgical procedures. After verification of loss of response to toe pinch, animals were placed in a stereotaxic frame (Stoelting) to perform the surgical procedures.

Mice used for comparison in this study had been anesthetized using ketamine–xylazine (KX) [12]. In our study, rats were anesthetized with ketamine–dexmedetomidine (KD) anesthesia due to the longer duration of cranial window surgery and tracer particle injection procedures, which typically require several hours. Xylazine is known to affect cardiac function and arterial pulsations in rodents and has been associated with increased complication rates in rats [56, 58, 59]. Rat data presented in this study were therefore acquired under KD anesthesia.

Cranial window surgery

Anesthetized animals were placed in a stereotaxic frame and head-fixed for cranial window surgeries. Hair was removed and the skull was exposed through a scalp incision. The periosteum from the exposed area of the skull was gently scraped away with a microsurgical blade, and a small amount of 10% ferric chloride was applied to the skull to completely dry the periosteum membrane and ensure that it has been removed completely. It is important that the skull is completely dry to ensure proper adhering of the glue and headplate. A craniotomy (approximately 5 mm in diameter) was then performed over the right middle cerebral artery vascular territory by using bregma, lambda, and the midline as reference points. Great care was taken not to damage the underlying dura. The craniotomy was filled with agarose (1.2% at 37 °C), covered with a glass coverslip, and sealed with cyanoacrylate glue. A custom headplate was then placed on the skull, and dental acrylic was used to cover exposed skull and keep the headplate in place.

Intracisternal cannulation and tracer infusion

Following the cranial window surgery, the cisterna magna cannulation procedure was performed as previously described with minor modifications [12, 13]. The atlanto-occipital membrane overlying the cisterna magna was exposed via a midline dorsal neck incision. A wound retractor was used to keep open the incision site. Then, a 30 G needle connected to a 4-cm long PE10 tubing filled with artificial CSF was advanced 1 mm into the intrathecal space via a small durotomy made using a 23-gauge needle. After carefully removing the wound retractor, the catheter was fixed to the dura with cyanoacrylate glue and dental cement, and the skin incision was closed around the catheter. Animals were monitored post-operatively and normothermia was maintained with a heating pad.

Immediately following the surgery, to visualize tracer movement from the subarachnoid space of the cisterna magna into the periarterial spaces, Alexa Fluor647-conjugated bovine serum albumin (BSA-647, 66 kDa, Invitrogen) and red fluorescent polystyrene microspheres (FluoSpheres 1.0 μL, 580/605 nm, Invitrogen) were diluted in artificial CSF at a concentration of 0.5% and 0.25% (w/v), respectively. Both tracers were briefly sonicated and loaded into a 100 μL Hamilton Gastight 1700 syringe (Hamilton) attached to a programmable syringe pump (Pump 11 Elite, Harvard Apparatus). The intracisternal catheter was then connected to the PE10 line filled with the tracers, and the tracers were co-infused into the rat cisterna magna at a rate of 2 μL/min over 5 min immediately before imaging. The infusion rate and volume of the CSF tracers were chosen based on previous findings showing no effect of this infusion rate on the measured CSF velocity [13].

In vivo two-photon laser scanning microscopy

A Chameleon Ultra II laser (Coherent) attached to a resonant scanner Bergamo scope (Thorlabs) and a × 20 (1.0 NA, Olympus) water immersion lens were used for in vivo two-photon imaging. To visualize the vasculature, fluorescein isothiocyanate (FITC)–dextran (2,000 kDa, 2.5%, Sigma-Aldrich) was injected intravenously via the femoral vein immediately before imaging. Intravascular and intracisternal fluorescent tracers were excited at 890 nm wavelength. Emission was filtered at 525, 607 and 647 nm. Images were acquired using ThorImage software at 30 Hz. Heart and respiratory rates were measured using an animal physiological monitoring device (Harvard Apparatus) which acquired measurements at 1 kHz and 250 Hz, respectively. The signals were digitized and recorded with a DigiData 1550A digitizer and AxoScope software (Axon Instruments), and synchronized with imaging acquisition using ThorSync software (Thorlabs).

Image processing and registration

Two-photon images were acquired with 512 by 512 pixel dimensions and 16 bit resolution. The 525-nm channel captured the vascular FITC-dextran. The 607-nm and 647-nm channels captured the red microspheres for particle tracking and BSA-647 CSF tracers, respectively.

All image processing and analysis was performed in Matlab 2023a. During image acquisition, arteries often exhibit small translational motion across the field of view associated with cardiac or respiratory pulsations. To remove movement artifacts, particle tracking videos were registered by cross-correlating artery location relative to a user-selected reference image to calculate displacement from the reference image in the ×and y directions. Images from all color channels were then sequentially read and rewritten with the rigid translations applied. The edges of each image are padded with zero-valued pixels such that all images in the registered video have the same spatial dimensions. Next, regions containing stagnant particles were masked from the image by the user to ensure only moving particles were used to calculate CSF flow speeds. A detailed description and tutorial of image processing is available [54].

Particle tracking

Particle tracking for each video was performed through an automated Particle Tracking Velocimetry (PTV) routine [54, 60, 61]. The algorithm identifies particle positions with sub-pixel accuracy, generating particle tracks and computing the velocity throughout the recorded video duration. Particle velocities were determined by convolution with a Gaussian smoothing and differentiating kernel. Some particles adhered to the artery or PVS walls, and thus no longer contributing to measurements of CSF flow, were eliminated by subtracting a dynamic background image specific to each frame. This background image was computed as the average of 300 frames before and after the given image.

Time-averaged velocities and speeds were derived by dividing the imaged area into a grid, as is shown in Fig. 1B and C. The mean speed for each experiment $\overline{S}$ was defined as the spatial mean of the time-averaged speed field. Here and throughout, we use overlines to indicate measurements of fluid and vessel motion averaged over space and time, but use brackets $\langle\cdot\rangle$ to indicate phase averaging (described below).

To calculate the root-mean-square velocity v_{RMS} at each instant in time, we computed the square root of the spatial mean of the square of all speed measurements. The downstream velocity component v_{down} was calculated as

$$v_{\mathrm{down}} = \mathbf{v} \cdot \mathbf{v}_{\mathrm{avg}}, \tag{1}$$

where $\mathbf{v}$ represents instantaneous particle velocity, and $\mathbf{v}_{\mathrm{avg}}$ is the unit vector field computed from the time-averaged flow field, aligned with the direction of arterial blood flow.

The mean downstream velocity $\overline{v}_{\mathrm{down}}$ is the average of v_{down} over time. The mean downstream velocity was also separated into retrograde and anterograde flow. Retrograde flow occurs when the downstream velocity is negative, meaning that fluid is moving opposite the direction of blood flow. The mean retrograde flow $\overline{v}_{\mathrm{down,r}}$ is the temporal mean of v_{down} when $v_{\mathrm{down}} < 0$. Conversely, anterograde flow is positive downstream flow. The mean anterograde flow $\overline{v}_{\mathrm{down,a}}$ is the temporal mean of v_{down} when $v_{\mathrm{down}} > 0$.

CSF motion is pulsatile, and the motion has previously been found to be correlated with arterial wall pulsations [12]. The cardiac pumping efficiency relates the directional flow to the oscillatory flow driven by cardiac pulsations. To isolate the cardiac pulsations from other pulsations, the downstream velocity measurements were

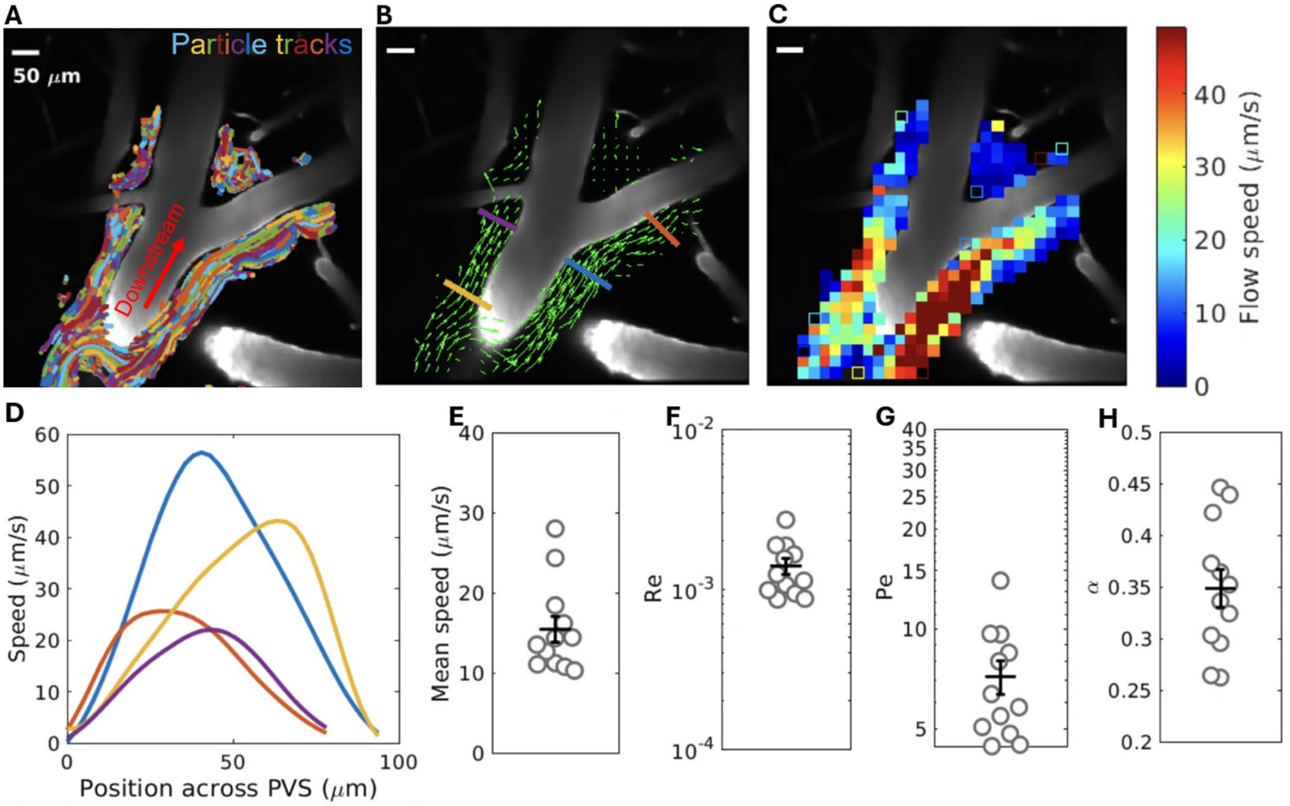

Fig. 1 An overview of CSF motion in the perivascular spaces of rats anesthetized with ketamine-dexmedetomidine. **A**) Superimposed particle tracks in a representative perivascular space. These particle tracks are used to produce **B**) The time-averaged velocity and **C**) The time-averaged speed. **D**) Time-averaged velocity profiles measured perpendicular to the artery at four cross sections, marked with colored lines in B). **E**) the mean speed, **F**) Reynolds number (Re), **G**) Péclet number (Pe), and **H**) Womersley number (α) for all experiments (plotted as open circles), along with mean ± standard error, *n* = *4 animals, n* = *12* samples. Videos of particle tracks from this example location are available in the supplemental material

filtered using a second-order Butterworth bandpass filter. The oscillatory flow v'_{down} was defined as the root-mean-square amplitude of downstream pulsations at the cardiac frequency, normalized by the mean downstream velocity:

$$v'_{\mathrm{down}} = \left(2T\int_0^T v_{\mathrm{down}}(t) - \overline{v}_{\mathrm{down}}\,dt\right)^{1/2}, \qquad (2)$$

where T is the length of the experiment and $v_{\mathrm{down}}(t)$ is the mean downstream velocity at each time. The pumping efficiency was then defined as $\eta = \overline{v}_{\mathrm{down}}/v'_{\mathrm{down}}$.

Phase averaging

To compare fluid quantities with cyclical physiological signals, CSF velocities were phase-averaged. Following the procedure described by [10], a physiological signal, typically either an ECG or respiration measurement, was used to define each cycle. Peaks in the physiological signal were identified using the Matlab function "findpeaks," and each peak was used to mark the start of a cycle. All times were then binned according to the fraction of the cycle elapsed since the most recent peak. CSF velocity measurements obtained concurrently were also binned according to the fraction of the cycle. The average waveform for each phase was interpolated onto the normalized time window. Thus, measurements were conditionally averaged according to the phase of the cycle at the moment they were recorded. For each experiment, the average waveform from all cycles was calculated along with the standard error of the mean.

To concurrently compare the impact of both respiration and cardiac cycles on fluid flows, v_{RMS} measurements were also conditionally averaged on both quantities simultaneously, according to the procedure of [62]. Using ECG waves and respiration measurements, values of v_{RMS} were binned into a two-dimensional matrix that specified the instantaneous measurement time with respect to both heartbeat and respiration. The data were used to create a surface plot that isolated the dependence of v_{RMS} on heartbeat and breathing, as is shown in Fig. 2B.

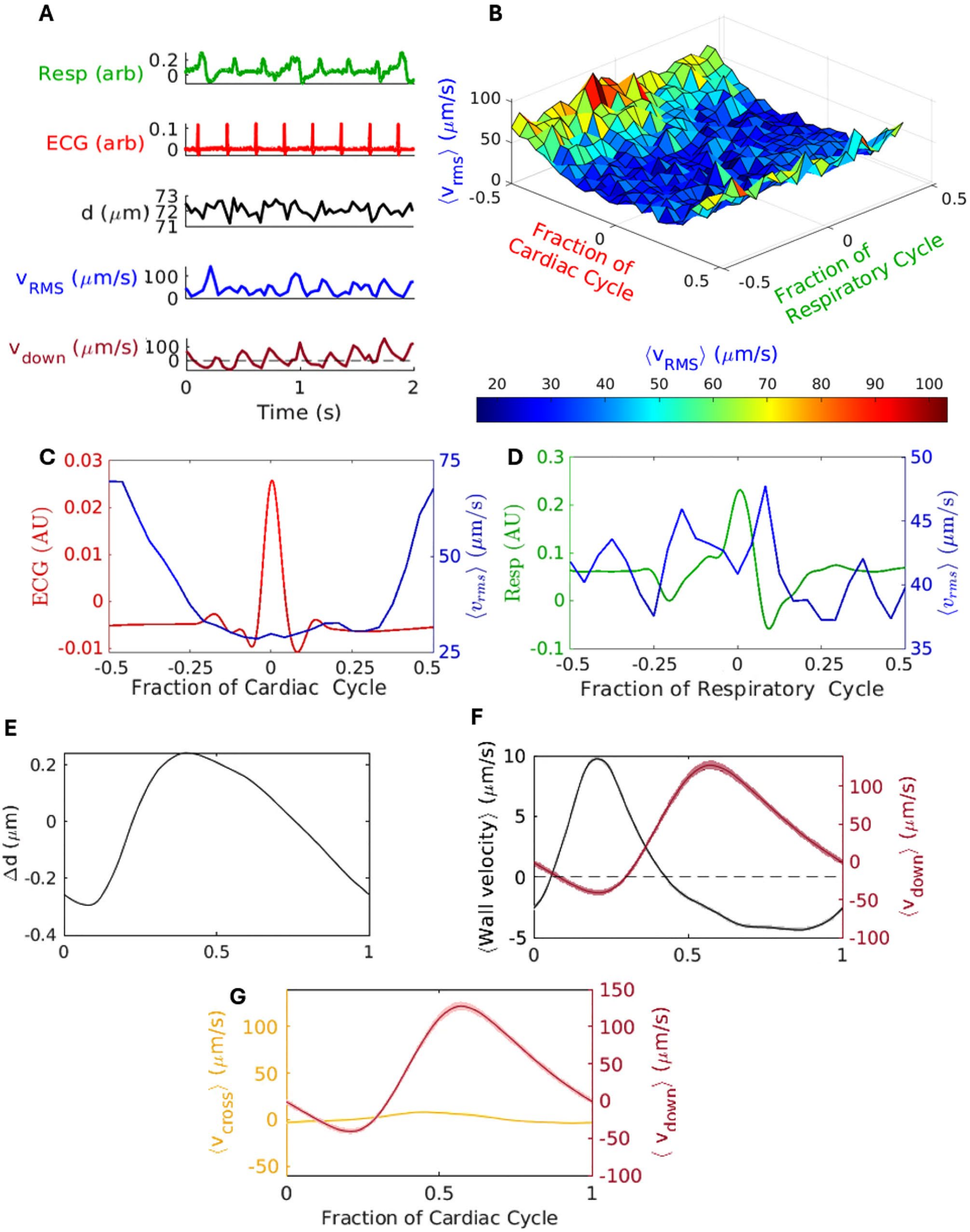

Fig. 2 (See legend on next page.)

(See figure on previous page.)

Fig. 2 Root-mean-square (v_{RMS}) and downstream velocity (v_{down}) fluctuate more with cardiac pulsations than with respiration. **A**) Representative samples of respiration (Resp), electrocardiogram (ECG), and artery wall diameter (d), along with root-mean square velocity and downstream velocity. **B**) v_{RMS} phase-averaged with respect to both the cardiac and respiratory cycles plotted together. **C**,**D**) v_{RMS} phase-averaged with respect to the cardiac and respiratory cycles, plotted on separate axes. In this experiment, the respiratory cycle was synchronized with the heart rate, which is common in anesthetized rats [63]. **E**–**G**) Deviations of d from its mean values, downstream velocity and artery wall velocity, and downstream velocity and cross-stream velocity (v_{cross}), all phase-averaged with respect to the cardiac cycle. **B**-**G**) Are phase-averaged following the procedure described in Section "Phase averaging"

Calculation of Reynolds number, Péclet number, and Womersley number

Fluid motion in the pial perivascular spaces was quantified using several dimensionless numbers. The Reynolds number (Re) was calculated as

$$Re = \frac{VL}{\nu}, \tag{3}$$

where V is the spatial mean of the time-averaged CSF velocity, L is the average PVS width (determined as described below), and $\nu = 0.697 \times 10^{-6} \mathrm{m}^2 s^{-1}$ is the kinematic viscosity of water at 36.8 °C.

The Womersley number (α) was calculated as

$$\alpha = L\sqrt{\frac{\omega}{\nu}}, \tag{4}$$

where ω is taken to be the angular frequency of the heart rate, since previous studies found that flows in pial PVSs oscillate primarily at the heart rate [10, 12].

The Péclet number (Pe), which quantifies the relative importance of advection and diffusion, was calculated as

$$Pe = \frac{VL}{D}, \tag{5}$$

where $D = 1.35 \times 10^{-10} \mathrm{m}^2 s^{-1}$, the value for monomeric amyloid-β [64], a naturally occurring solute in the brain. However, the diffusion coefficient for the 1 μm beads used in this experiment is $D = 6.55 \times 10^{-13} \mathrm{m}^2 s^{-1}$, increasing the Péclet number of the solute used for particle tracking velocimetry by a factor of approximately 200.

Measurements of the shapes of perivascular spaces

Segmentation of PVSs and vessels was performed using the procedure and algorithms described by [15]. The boundaries of PVSs and arteries were obtained using the EdgeFinder algorithm, which determined the threshold for the edge of the channel at each depth based on the maximal magnitude of the gradient. Frequently, nearby vessels or PVS regions were identified by this algorithm. To remove those channels from the segmentation, only the largest connected region in the vessel segmentation and the two largest regions in the perivascular space (PVS) segmentation were retained. Further refinement involved the manual removal of vessels branching off the main vessel of interest. The resulting segmentation was then compared with the original image, and the threshold was refined iteratively until the segmentation agreed closely with the original image.

Cross-sectional images normal to the vessel were created to measure the area of the perivascular spaces. While the distance between cross sections varied depending on the curvature of the artery, the average distance was approximately 1 μm. The vessel centerline was identified using the "bwskel" function in Matlab, which iteratively thins the segmented artery to find points in the center of the binary object. Each cross section was analyzed separately for calculations of hydraulic resistance and simulations of flow.

Calculations of hydraulic resistance and flow fields

Hydraulic resistance per unit length was calculated in each normal cross section. This calculation assumes that the flow in a cross section is Poiseuille flow, which is unidirectional and fully developed. The bending of the perivascular space or variations in artery wall diameter do induce off-axis flow components, potentially elevating hydraulic resistance. However, the magnitude of off-axis flow is small in relative to axial flow [10]. Disregarding off-axis components, we calculated hydraulic resistance by solving Poisson's equation for dimensionless steady flow in a pipe [22]. We solved Poisson's equation with Matlab's "solvepde". To calculate hydraulic resistance for each segmented PVS, we used the "polyshape" and "geometryFromMesh" functions to create a discretized mesh. We refined the mesh until the element size was small enough that the error in resistance for a circle of the same area was less than 1%. We then numerically solved for flow of water at 36°C, which has a viscosity of 7.06×10^{-4} Pa s.

While hydraulic resistance is independent of fluid conditions, to simulate dimensional flow, a pressure gradient must be selected. As there is no estimate of pressure gradients in rat PVSs, for both species a pressure gradient was selected such that the mean velocity throughout all simulations would match with the mean downstream velocity measured experimentally (Fig. 4D).

Statistical analysis

To all quantities of interest compared in rats and mice, statistical tests were performed in Matlab using the function "ttest2" with the assumption of unequal variances.

Normality was tested using Lilliefors tests. When normality was not met, hypothesis testing was performed with the Matlab function "ranksum," which returns the *p*-value of a two-sided Wilcoxon rank sum test, a non-parametric test. As most distributions were normal, the few *p*-values from Wilcoxon tests are reported with (Wilcoxon). All hypothesis testing was two-tailed.

On plots, statistical significance is presented using astrices using the standard notation: * indicating $0.01 < p < 0.05$, ** indicating $0.001 < p < 0.01$, *** indicating $0.0001 < p < 0.001$, and so on. Exact *p*-values of at least a 0.05 level of significance are stated.

Results

Average CSF motion in rat PVSs

First, we set out to measure the mean flow in pial PVSs of rats. CSF flow was measured using tracer particles tracked in recordings spanning 5 to 10 minutes, and measurements from a typical recording are shown in Fig. 1A-C. On average, CSF in rat PVSs flows in the same direction as blood (Fig. 1B), as it does in mice. The flow is fastest in the center of the PVSs, and the velocity approaches zero at solid boundaries of the artery wall and PVS outer wall (Fig. 1D), indicating that pial PVSs in rats are open (rather than porous), as they are in mice [1214].

Considering flows in the PVSs of all rats and averaging over both space and time, the mean speed of the fluid is 15.4 μ m/s with a standard error of 1.6 μ m/s, as there is variation among individual rats and among different locations along the MCA of the same individual (Fig. 1E). The mean Reynolds number is 1.4×10^{-3} with a standard error of 0.16×10^{-3} (Fig. 1F), indicating that flow is laminar, not turbulent. For monomeric amyloid-β, the Péclet number is typically between 5 and 10, with a mean value of 7.2 (Fig. 1G), indicating that advection dominates even for highly diffusive naturally occurring solutes. (the Péclet number is larger for larger molecules, like tau.) Additionally, the Womersley number α is approximately 0.35 with a standard error of 0.018 for the frequency of the heartbeat. When the Womersley number is less than 1, viscous forces dominate the transient inertial forces caused by pulsations (Fig. 1H).

CSF dependence on cardiac cycle and respiration

In mice, it has been shown that CSF flow through pial PVSs has pulsations dominated by the frequency of the cardiac cycle, not respiration [12]. To identify the extent to which cardiac and respiratory pulsations drive flow in rat pial PVSs, we phase-averaged our measurements of CSF flow speed with respect to both cardiac and respiratory measurements, as described in "Phase averaging"

Figure 2A-D show v_{RMS} phase-averaged with respect to ECG and respiration. It is clear that when phase-averaged, $\langle v_{\mathrm{RMS}} \rangle$ correlates strongly with the cardiac cycle and weakly with the respiration cycle. Although the respiratory correlation is complicated by the synchronicity of the cardiac and respiratory cycles, there is a noticeable peak in $\langle v_{\mathrm{RMS}} \rangle$ immediately after each breath. This indicates that within rat pial PVSs, cardiac pulsations drive most flow, but respiration can still influence CSF inflow rates.

This correlation between the cardiac cycle and fluid motion is apparently driven by the motion of the artery wall. Figure 2E shows the variation of the artery diameter over one cardiac cycle. Figure 2F further shows that the downstream velocity $\langle v_{\mathrm{down}} \rangle$ decreases while the artery is expanding, with most anterograde flow occurring as the artery is constricting as part of its cardiac-driven diameter oscillation. A similar correlation between CSF velocity and artery wall velocity was observed in mice [12], although in mice, peaks in CSF inflow occur concurrently with peaks in artery wall velocity. Lastly, Fig. 2G indicates that the downstream velocity is substantially larger than the cross-stream velocity throughout the cardiac cycle, confirming that axial pulsations with the heart rate do not affect measurements of v_{RMS}.

Rat perivascular geometry

Now we consider rat PVS shapes. Rat perivascular spaces were segmented following the procedure described in [15], and sample segmentations are shown in Fig. 3A-C. From these segmentations, the hydraulic resistance per unit length was calculated in each cross section.

Figures 3D and E show the distributions of hydraulic resistance and PVS area across all cross sections segmented from z-stacks. Along the middle cerebral artery, the hydraulic resistance per unit length is almost always between 10^{14} and 10^{15} Pa $\times$ s / m^4, and the area of the pial perivascular space is between 10^4 and 4×10^4 $\mu\mathrm{m}^2$. These areas are nearly ten times larger than in mice [15].

The dependence of hydraulic resistance on PVS area is shown in Fig. 3F. Hydraulic resistance decreases as cross-sectional area increases, following a power law with exponent −2.12. A similar relationship between artery area and PVS hydraulic resistance was found in mice [15], allowing hydraulic resistance to be accurately predicted for a known area without further simulations. In mice, the exponent is −1.73. Thus, PVS hydraulic resistance is more sensitive to cross-sectional area in rats than in mice.

Comparison of CSF motion in rats and mice

In the previous sections, CSF speeds and PVS geometries in rats were qualitatively compared to mean CSF flows reported in mice from previous publications. Here, the flows are compared quantitatively, and the relationship between CSF flow and PVS size in the two species is tested for significance using data from rats and a sample

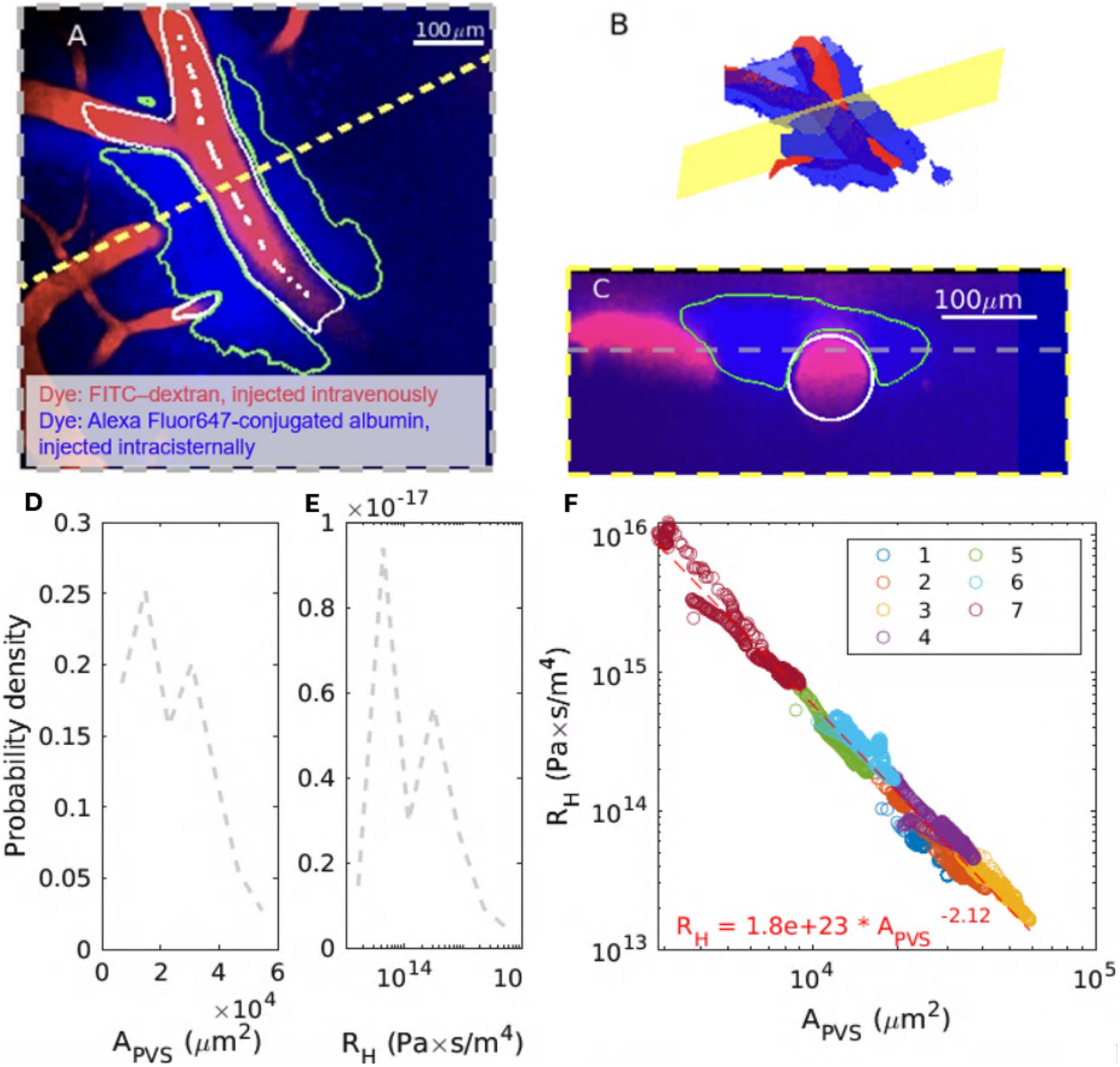

Fig. 3 Segmentations of perivascular spaces (PVSs) in rats are used to explore the relationship between hydraulic resistance and PVS area. **A**) One image with segmentation overlaid. White and green curves enclose regions identified as arteries and PVSs, respectively. **B**) Three-dimensional rendering of the segmented arteries and perivascular spaces. **C**) Image in a plane normal to the artery, with segmentation overlaid. The location of this plane is indicated in yellow in (**A**–**B**). **D**–**E**) Probability density functions of hydraulic resistance and cross-sectional area, respectively, were calculated from many cross-sections of PVSs. **F**) Hydraulic resistance (R_H) decreases with PVS cross-sectional area (A_{PVS}) in seven different PVSs (plotted in different colors). A power-law fit for the entire data set is also shown

of ten wild-type mice. These mice were anesthetized using ketamine/xylazine, using procedures described previously [12, 13], and prepared using the same surgical procedure used for rats.

The magnitude of mean speed, previously presented in Fig. 1E, was approximately the same for both species (Fig. 4A). In previous experiments, as well as in Fig. 1, mean speed has been used to calculate the Reynolds number and Péclet number in pial PVSs [12, 13]. We also calculated the average downstream velocity $\overline{v}_{\mathrm{down}}$, which involves the velocity component parallel to the artery but excludes the lateral (cross-stream) component. We found that $\overline{v}_{down}$ was also approximately the same in mice and rats (Fig. 4B). However, the pumping efficiency, defined as the mean downstream velocity normalized by the root-mean-square amplitude of velocity, was much lower in rats than in mice [65]. CSF flows in pial PVSs of

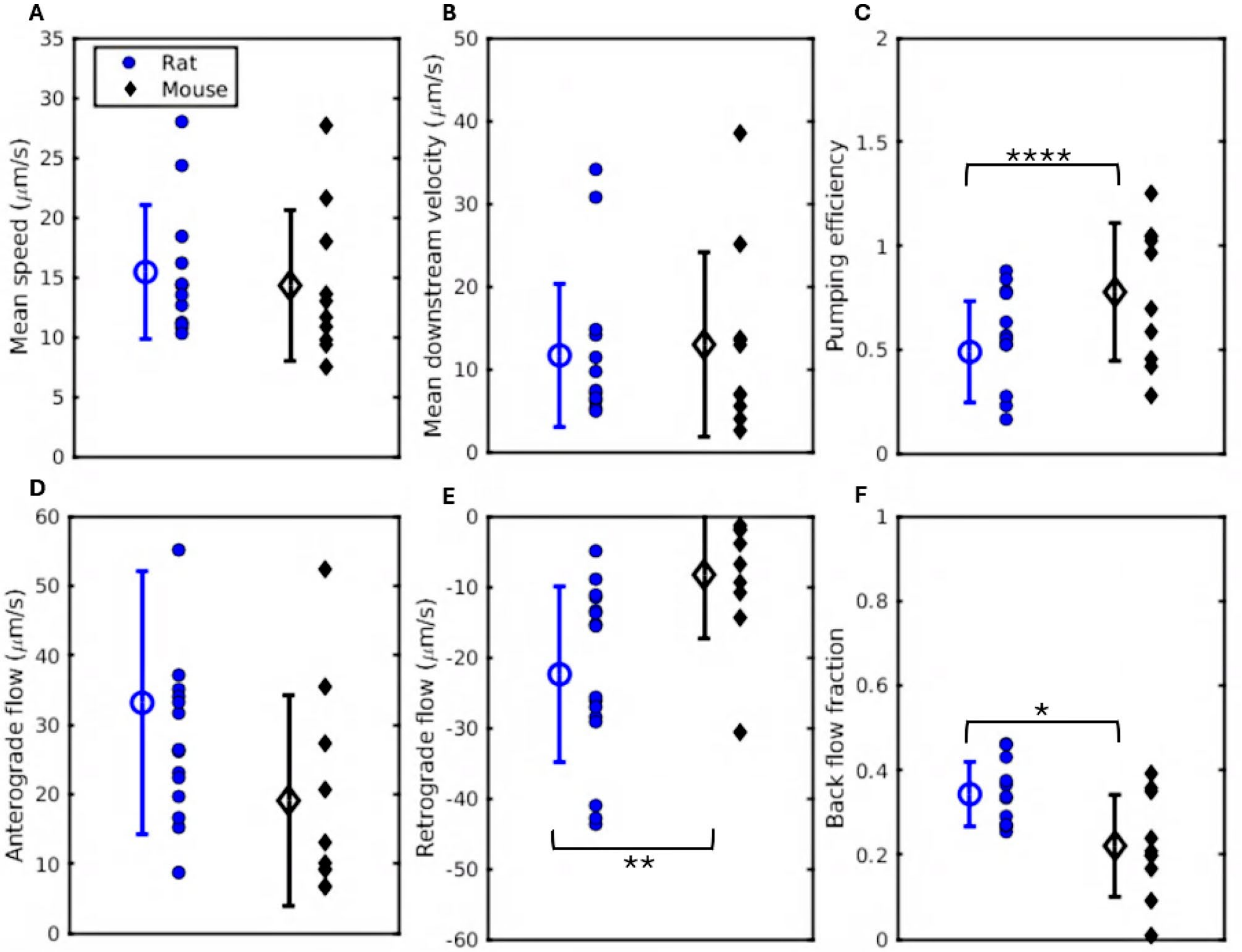

Fig. 4 CSF motion in rats (blue) and mice (black). **A**) Mean flow speeds in pial perivascular spaces of rats and mice are not statistically different. **B**) The mean downstream velocity is also not different (Wilcoxon). **C**) The pumping efficiency of cardiac pulsations, which is the ratio of downstream velocity to the amplitude of pulsations, is lower in rats than mice (0.49 vs 0.78, $p = 0.0001$). **D**–**E**) The mean flow in the direction of blood flow is not statistically different (Wilcoxon), while the mean flow in the opposite direction is statistically different between rats and mice ($p = 0.0061$). **F**) Flow is retrograde for a greater fraction of time in rats than in mice (0.34 vs 0.22, $p = 0.028$). *rats: n = 4* animals, *n* = 12 samples, mice: *n* = 10 animals, *n* = 10 samples

rats are more pulsatile relative to the mean downstream velocity (Fig. 4C).

To characterize the flow in greater detail, we separately considered the times when CSF flow was anterograde (in the same direction as blood flow) and retrograde (in the opposite direction), calculating the mean velocity for each (Figs. 4D and E). While the anterograde flows are similar, the retrograde flows are faster in rats. Additionally, there was a greater backflow fraction in rats, meaning that the retrograde flow occurs for a larger portion of the cycle (Fig. 4F).

Comparison of perivascular spaces and calculated flow rates

The geometry of the perivascular spaces is important for modeling fluid motion. In particular, the areas and hydraulic resistances of perivascular spaces are used in simulations of fluid motion in perivascular spaces [21, 22]. The geometries and resistances of pial PVSs in rats and mice are characterized in Fig. 5 A-C. The PVS area is significantly larger in rats than mice, and as a result, the hydraulic resistance per unit length of PVS is significantly lower in rats than in mice (Fig. 5A,B). Consistent with the representative example shown in Fig. 1, quantitative measurements in Fig. 5B show that the mean pial PVS cross-sectional area typically exceeds the artery cross-sectional area in rats as well as mice. While the artery diameters along the MCA are similar in the locations sampled in this study, the average diameter is larger in rats than in mice.

A valuable quantity for understanding fluid transport is the volume flow rate $Q = \overline{v}_{\mathrm{down}} A$, where A is the area of a cross section and $\overline{v}_{\mathrm{down}}$ is the mean velocity through that cross section (averaged over both space and time).

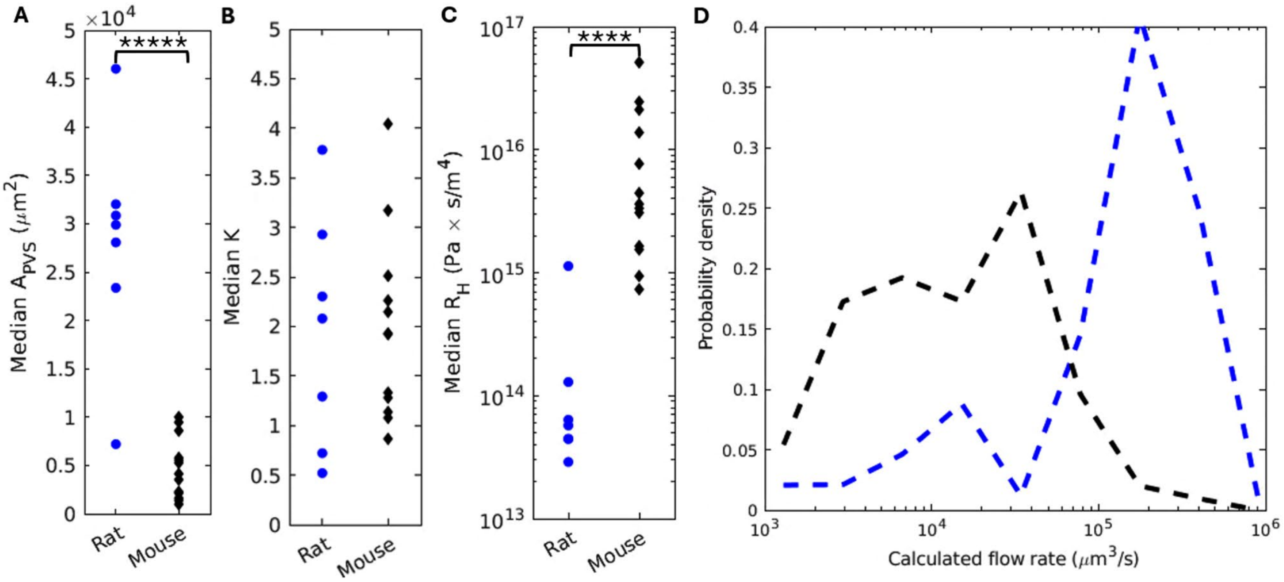

Fig. 5 The geometry of perivascular spaces (PVSs) in mice and rats, and the resulting volume flow rates. **A**) Median cross-sectional area (A_{PVS}) for each PVS. Rat PVSs have larger cross-sectional area than mouse PVSs ($p < 0.00001$). **B**) Although the cross-sectional areas are different, the area ratio (K), defined as the PVS area normalized by the artery area, is not different in rats and mice ($p = 0.859$). **C**) Median hydraulic resistance (R_H) for each PVS. Rat PVSs have a mean hydraulic resistance more than an order of magnitude lower than mouse PVSs ($p < 0.0001$, Wilcoxon). **D**) Distributions of calculated volume flow rates through all PVS cross-sections in rats and mice. The mean volume flow rate in rats is $1.7x10^5$ μm/s, 3.0 times larger than in mice ($5.7x10^4$ μm/s, p<0.00001, Wilcoxon). Although the average flow speed is slower in rats, the larger area allows for a greater volume of fluid to pass

We measured the mean downstream velocity to be 11.6 μm/s in rats and 13.0 μm/s in mice (Fig. 4B). Based on those measurements of $\overline{v}_{\mathrm{down}}$, the calculated volume flow rates through each segmented cross section in both mice and rats are shown in Fig. 5D. Although the downstream velocity is lower in rats, the volume flow rate is three times greater.

Comparing rats and mice under different anesthetics

Finally, we compared CSF and arterial pulsation in rats anesthetized with KD with rats and mice anesthetized with KX (Fig. 6A and B). The pulsations of the artery wall and the corresponding downstream CSF flow were analyzed by examining frequency bands of interest, isolated using second-order, bandpass Butterworth filters. We quantified pulsations of vessel diameter and downstream CSF velocity in each frequency band with the interquartile range (IQR) of the filtered data, normalized by the mean (Fig. 6C and D).

First, we compared pulsation at the slow vasomotion range. This frequency band spanned from 1/60 Hz to 1/10 Hz, approximately the range of slow vasomotion frequencies observed in KX rats (Fig. 6A). Figure 6C shows that arteries exhibit more pulsation in this frequency band when rats are anesthetized with KX instead of KD ($p = 0.0001$, Wilcoxon). Additionally, rats anesthetized with KX have more pulsatile arteries in the slow vasomotion band than mice do ($p = 0.0001$, Wilcoxon). However, KD rats and KX mice do not have significantly different slow vasomotion ($p = 0.28$). Correspondingly, there are differences in CSF pulsation at slow vasomotion frequencies (Fig. 6D). KX anesthesia results in significantly more pulsatile CSF flows at low frequencies in KX rats compared to KD rats ($p = 0.0035$, Wilcoxon). Even still, CSF flows in mice are slightly less pulsatile than flows in KD rats at this frequency band ($p = 0.028$, Wilcoxon), and are much less pulsatile compared to KX rats ($p = 0.0003$).

The second band of interest spanned from 0.2 Hz to 0.8 Hz for rats and from 0.1 Hz to 0.4 Hz for mice, encompassing the Mayer wave frequencies [66]. Mayer waves are indicative of sympathetic nervous activity which can be affected by anesthesia. Arterial pulsation at the Mayer wave frequency band are different between KD rats and mice ($p = 0.016$), but there is no difference in the corresponding CSF flows. Otherwise, arterial pulsation in this range are not significantly affected by anesthesia type or species. This indicates that the animals were sufficiently anesthetized during our experiments [67]. That finding is consistent with our observations that frequent toe pinches during experiments failed to arouse the rats. Following the trend observed in all frequency bands, KX rats exhibit significantly higher CSF pulsations compared to KD rats ($p = 0.0002$) or mice ($p = 0.0001$, Wilcoxon).

The final band of interest spanned from 2 Hz to 8 Hz, encompassing the cardiac frequency (for either rats or mice, when anesthetized). There are no significant differences in arterial pulsation between the three groups. CSF speed, however, was more pulsatile in rats than in mice,

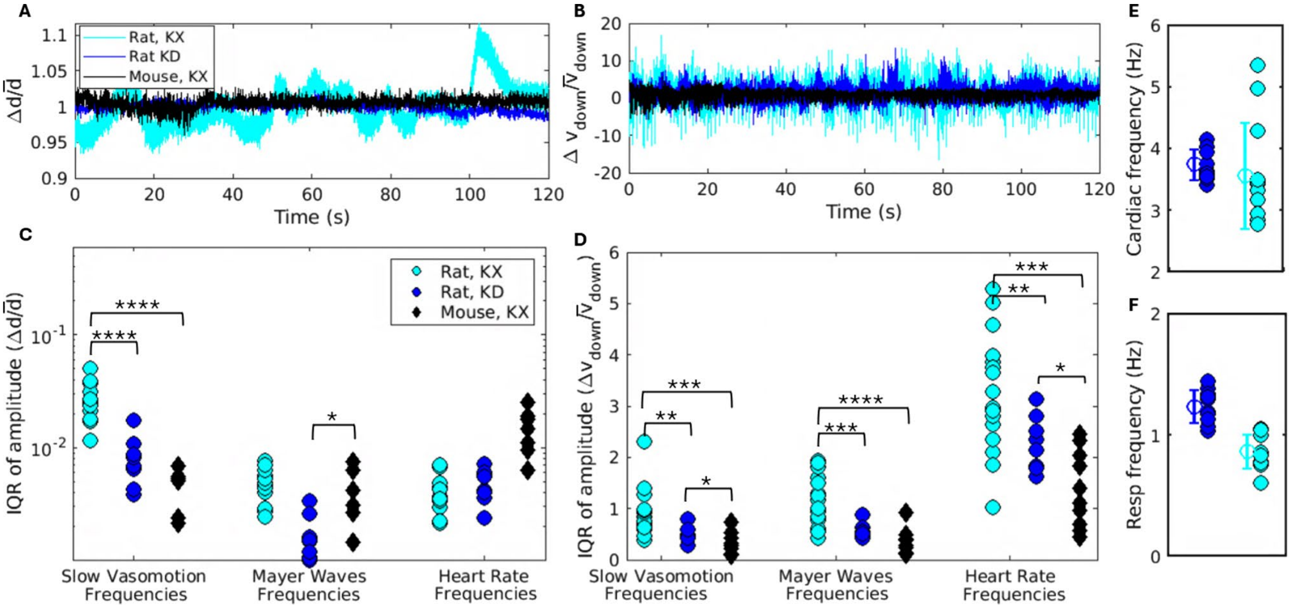

Fig. 6 Quantification of arterial pulsations and corresponding cerebrospinal fluid (CSF) motion for rats and mice under different anesthetics. **A**) Variation of normalized artery diameter $d/\overline{d}$ (where d is diameter and $\overline{d}$ is its long-term mean) for a representative rat and mouse. **B**) Variation of normalized downstream velocity $v_{\mathrm{down}}/\overline{v}_{\mathrm{down}}$ (where v_{down} is downstream velocity and $\overline{v}_{\mathrm{down}}$ is its long-term mean) for a representative rat and mouse. **C**) Interquartile range of $d/\overline{d}$ in three frequency bands for rats and mice. A larger value for interquartile range normalized by its mean indicates greater pulsatility. **D**) Interquartile range of $v_{\mathrm{down}}/\overline{v}_{\mathrm{down}}$ for the same three frequency bands. **E**) and **F**) Show the mean frequency of the cardiac and respiration cycles for rats anesthetized with KX and KD in separate recordings of physiological signals, along with the mean and standard deviation of those measurements. *KX rats:* $n=4$ animals, $n=16$ samples, KD rats: $n=4$ animals, $n=12$ samples mice: $n=10$ animals, $n=10$ samples

both when the rat was anesthetized with KD ($p=0.010$) and KX ($p=0.0004$, Wilcoxon). As in other frequency bands, KX rats have more pulsatile CSF flows than KD rats ($p=0.0059$). In both species, the strongest CSF pulsations occurred in the cardiac band. This is consistent with the results of phase averaging (Fig. 2).

Lastly, Figs. 6E and F show that KX and KD anesthesia affects heart rate and respiration differently in rats. While the mean cardiac frequency is similar regardless of anesthetic, heart rates are more variable when rats are anesthetized with KX. Additionally, respiration rates are much lower and more variable when rats are anesthetized with KX. The large spread of cardiac rates for rats anesthetized with KX suggests that the animals' responses to the anesthetic are less predictable.

Discussion

This paper presents high-fidelity, in vivo measurements of CSF flow in rat pial PVSs, prior to penetration into the cortical surface, via automated particle tracking, as well as statistical characterization of the sizes and hydraulic resistances of those PVSs. Although the flows in and geometries of mouse pial PVSs have been extensively quantified, no such study has been previously undertaken in rats. Studies are performed on model animals whose glymphatic function and dysfunction, it is hoped, can give information that is useful for improving human health and clinical outcomes. Rats, being approximately 10 times larger than mice and with more complex brains, provide a intermediate species between mice and humans. It seems useful, then, to compare and contrast glymphatic function in these two different rodent species. We found that CSF volume flows, but not speeds, are faster in rats than mice (Fig. 4). Additionally, the ratios of PVS area to artery area are similar in both species, resulting in rats having much larger, lower resistance pial PVSs which facilitate the faster CSF volume flows (Fig. 5). These results can aid researchers in scaling their measurements of CSF flows in mice to make predictions about CSF behavior in humans. Important similarities and differences between rats and mice are summarized in Table 1.

Similarities among species

We identified several commonalities among both species. We found that the Reynolds number is approximately 10^{-3} in rats, on the same order of magnitude as what has been observed in mice [12]. While the relative strength of advection and diffusion varies below the brain's surface [71], we found that in pial PVSs, the Péclet number for naturally occurring solutes is much larger than 1, indicating that solute transport is advection-dominated. The velocity profile of the fluid is approximately parabolic, indicating that pial PVSs are open, not porous, as in mice [14]. Furthermore, both the mean flow speed (Fig. 4A) and the area ratio K of PVS area to artery area is

Table 1 A comparison of physiological signals, CSF flows, and pial PVS geometries in rats and mice. Values without a citation were quantified in this study. Unless otherwise specified, single-number values are medians. If measured values are statistically different, the ratio of rats:mice is also reported

	KD Rat	**KX Mouse**	**Ratio**
Brain CSF volume	156μL [40]	35μL [39]	4.5
Brain mass	2 g [68]	0.4 g [69]	5
CSF production rate	325 nL/min [38]	90 nL/min [70]	3.5
Cardiac frequency	2.8–5.2 Hz	2.7–4.3 Hz	-
Respiration frequency	0.8–1.3 Hz	0.7–1.0 Hz	-
Reynolds number	1.5×10^{-3}	$1 \times 10^{-3} : 1 \times 10^{-4}$ [12]	-
Mean speed	15.4μm/s	14.3μm/s	-
Mean anterograde flow	33.15μm/s	19.0μm/s	-
Mean retrograde flow	–22.4μm/s	–8.3μm/s	2.7
Mean downstream CSF velocity	11.6μm/s	13.0μm/s	-
Backflow fraction	0.34	0.22	1.5
Cardiac pumping efficiency	0.49	0.78	0.63
PVS area	$2.6 \times 10^{4} \mu$m^2	$4.7 \times 10^{3} \mu$m^2	3.9
Hydraulic resistance	1.8×10^{14} Pa×s/m^4	3.5×10^{15}Pa×s/m^4	0.05
CSF volume flow rate	$1.7 \times 10^{5} \mu$m^3/s	$5.7 \times 10^{4} \mu$m^3/s	3.4

approximately the same (Fig. 5B). For both species, flow in pial PVSs pulses much more strongly at the cardiac frequency than at the respiratory frequency, suggesting that artery wall motion is a strong flow driver. Importantly, this result is influenced by the proximity of the CSF measured to the moving boundary of the artery wall.

Differences between species

We also identified several important differences in glymphatic function between rats and mice. While cardiac pulsations do drive flow in rats, the relationship between $\langle v_{\mathrm{RMS}} \rangle$ and wall pulsation is different in rats than in mice. In mice, increases in v_{RMS} typically coincided with peaks in wall velocity [12], whereas in rats, peaks in v_{RMS} typically coincide with minima in the wall velocity. In mice, as the artery expands, CSF is pushed in the same direction as blood, and the increase in anterograde flow causes the peak in v_{RMS} [12]. More broadly, in mice, slow, high-amplitude artery wall motion has been shown to drive downstream volume flows [72]. However, in rats, v_{RMS} is maximum while the artery is constricting (Fig. 2). The observed spike in CSF flow rates in pial PVSs during local artery constriction in rats differs from what has been reported in mice, but resembles the large-scale CSF and blood dynamics observed in humans. Human MRI studies have shown that brain-wide CSF flow is fastest during arterial constriction [32, 73, 74]. In rats, we also observed a modest correlation between respiration and CSF inflow, whereas no such correlation is apparent in mice [12]. Together with the phase shift between CSF inflow and arterial wall motion, these findings suggest that CSF efflux from the nearby subarachnoid space may contribute measurably to pial PVS flow in rats, but not in mice. This could be caused by the lower hydraulic resistance of pial PVSs in rats (Fig. 5C), allowing smaller pressure gradients to drive measurable flows in these PVSs.

CSF flows are more pulsatile across all frequency bands in rats than in mice. We argue that this occurs because rat PVSs have lower hydraulic resistances compared with mouse PVSs (as we have measured). That is, flow can be driven more easily, even by relatively small artery wall pulsations. Note that the Womersley number is much less than 1 for all frequency bands (Fig. 1F), and its low value indicates that transient inertial effects are negligible, so the steady hydraulic resistance is also applicable to pulsatile flow.

Physiological interpretation of results

We observe slightly slower net, directional flow in rats than in mice (Fig. 4). However, the rat pial PVSs are nearly an order of magnitude larger than those measured in mice (Fig. 5). As a result, the volume flow rate through rat PVSs is approximately 3.0 times larger (Fig. 5). CSF production rates in rats exceed those of mice by a similar ratio, as shown in Table 1. Although it is unclear what fraction of CSF flows through PVSs versus other pathways, the comparable ratios of CSF production to PVS flow across species suggest that a consistent fraction of CSF enters PVSs relative to other routes [75, 76]. Experiments on additional species are needed to confirm this scaling, as there is uncertainty about what pathways, other than PVSs, may lead to these efflux routes [77].

Importantly, while the PVSs in rats are much larger than in mice, there is no statistical difference between their area ratios (Fig. 5B). Arteries along the brain surface are much larger in rats than in mice, with similarly enlarged PVSs. While noninvasive imaging of healthy PVSs in humans remains challenging, we conjecture that it is reasonable to approximate human pial PVSs as having an area ratio in the range of 0.5–4 times the area of human pial arteries.

Effects of anesthesia

Finally, we observed that the choice of anesthetic significantly affects vasomotion and corresponding CSF motion in rats (Fig. 6). Rats anesthetized with KX had strong vessel pulsations at frequencies below the normal cardiac range, and correspondingly pulsatile CSF motion. Rats anesthetized with KD exhibited vasomotion and CSF pulsations more similar to what has previously been observed in KX-anesthetized mice. Additionally, physiological signals were less variable in KD rats compared with KX rats, suggesting that rats respond more predictably when anesthetized with KD for long intervals. This is consistent with previous studies that dexmedetomidine is more selective for alpha-2 receptors than xylazine is [57], decreasing vasomotion and resulting in less variability in heart rates [78]. Thus, we recommend future experiments requiring multiple hours of anesthesia be performed under KD, rather than KX. Future work exploring vessel and CSF pulsatility in mice anesthetized with KD, KX, and other anesthetics is still needed.

Future experimental work

All animals considered in this study were anesthetized, but there are significant differences between anesthesia and natural sleep or wake states. Brain-wide solute transport is much more efficient during natural sleep than during wakefulness, as is CSF transport [3]. It has been hypothesized that enhanced metabolic waste clearance during sleep is a biological driver for sleep [2]. Many features of natural sleep, particularly slow-wave oscillations, closely couple to the size of brain interstitial spaces, which then influences the corresponding volume flow rate of CSF [3]. However, slow-wave oscillations are suppressed under anesthesia [55]. Furthermore, anesthesia is known to alter rodent hemodynamics, changing blood pressure, mean arterial pressure, and artery diameter [79, 80]. Diameter changes are known to affect CSF motion in PVSs [72]. Future comparisons of naturally sleeping rats to mice would offer additional insight into CSF dynamics and the coupling of CSF flows and vessel pulsations. This is particularly important given that KX anesthesia appears to allow more low-frequency vessel pulsation in rats than in mice. In addition, studies examining other types of PVSs, especially those surrounding smaller pial arteries and penetrating arterioles, will be important to determine whether the relationships observed here generalize across the brain's vasculature. Computational models suggest that penetrating PVSs play a key role in delivering CSF to brain tissue and clearing metabolic waste [17, 71], but these predictions are limited by large uncertainties in PVS size and permeability. Additional experimental measurements of penetrating PVSs are needed to confirm that CSF flowing in pial PVSs perfuses brain tissue.

Conclusion

Animal models are frequently used to explore biological phenomena, and those results then inform our understanding of human health and disorders. One benefit of rodent experiments is the availability of transgenic mice, which are genetically engineered to study different diseases and cancers [81, 82]. Additionally, invasive and highly controlled animal experiments, which would be unethical or impossible to perform on humans, provide a valuable contribution to scientific research [83, 84]. However, to appropriately apply information obtained through animal experiments to human treatment plans, it is necessary to understand how biological systems scale between species. Scaling laws are ubiquitous in biology, and frequently can be attributed to the scaling of fundamental laws of heat and mass transfer with animal size [85, 86]. We found that CSF volume flow rates in pial PVSs appear to scale with CSF production rates in the two species, although further experiments on additional species are needed to confirm that scaling.

We quantified several aspects of CSF flow that are necessary for creating accurate and detailed models. The mean downstream velocity in rats is 12 μm/s, lower than the 20 μm/s previously observed in mice [12, 72]. We also quantified the hydraulic resistance and PVSs in both species, finding larger, lower resistance PVSs in rats compared with previous measurements in mice [15]. The relationship between hydraulic resistance and area has previously been used to create hydraulic network models of PVSs in mice, which can calculate flow rates even through networks of channels with poorly defined geometries [21]. These measurements may be used to produce new models of flow in rat PVSs, which can be compared with the many existing studies on rats that used MRI to explore brain-wide transport [25, 50, 87, 88].

In the future, simulations or machine learning techniques can use the measured pial PVS geometries and CSF flows to better estimate the pressure variations needed to drive flow in both species [10]. These measurements can then offer insight into possible differences in material properties of the membranes surrounding PVSs in rats and mice. Such studies may be able to explain the phase shift between CSF inflow and artery wall motion shown in Fig. 2, which was not observed in mice. Further research on animals that are more similar to humans, such as pigs and sheep, would also be beneficial. Humans produce approximately 500 mL of CSF per day and have a turnover time of approximately 8 hours [89], compared to approximately 2 hours in mice and rats [90].

Furthermore, humans have folded (gyrencephalic) brains, mice and rats have smooth (lissencephalic) brains, and brain folds correlate with higher CSF influx rates [91]. Additionally, the relative ratio of cell types that compose brain tissue is very different in humans and rodents [92]. Using similar experimental techniques to explore a variety of species remains important as we apply our analysis of animal models to treatments of human disorders.

Supplementary information

The online version contains supplementary material available at https://doi.org/10.1186/s12987-026-00782-w.

Supplementary Material 1

Acknowledgements

The authors would like to acknowledge the contributions of Kimberly Boster and Nikola Raicevic in developing the z-stack segmentation functions and analyzing the z-stacks of pial PVSs in mice. We would like to acknowledge Jeff Tithof for developing and documenting the procedure for particle tracking in mice, and for tracking CSF flows in several of the mice used in this study.

Funding

This research was supported by grants from the U.S. Army (MURI W911NF1910280), the National Institutes of Health (U19NS128613, R01AT012312) the Lundbeck Foundation, (R386–2021–165), the Novo Nordisk Foundation (NNF20OC0066419), The Simons Foundation (811237); and Dr. Miriam and Sheldon G. Adelson Medical Research Foundation.

Data availability

All experimental data presented in this paper are available at https://dandiarchive.org/dandiset/001045.

Declarations

Ethics approval and consent to participate

Experiments were performed according to guidelines of the United States National Institutes of Health, and protocols were approved by the University of Rochester Committee on Animal Resource (UCAR) (Protocol 2011–023).

Competing interests

The authors declare no competing interests.

Author contributions

K.Q. analyzed and interpreted data. A.L.G. performed experiments. K.Q. and A.L.G wrote the manuscript. A.R. developed analyses and performed analysis of mouse experiments. H.M. performed experiments on mice. M.N. and D.H.K. conceived of the study and oversaw animal experiments and data analysis, respectively. D.H.K oversaw the writing of the manuscript. All authors reviewed the manuscript.

Received: 23 July 2025 / Accepted: 18 February 2026

References

1. Iliff JJ, Wang M, Liao Y, Plogg BA, Peng W, Gundersen GA, et al. A paravascular pathway facilitates csf flow through the brain parenchyma and the clearance of interstitial solutes, including amyloid β. Sci Transl Med. 2012;4(147):147–111147111.
2. Benveniste H, Heerdt PM, Fontes M, Rothman DL, Volkow ND. Glymphatic system function in relation to anesthesia and sleep states. Anesth Analg. 2019;128(4):747–58.
3. Xie L, Kang H, Xu Q, Chen MJ, Liao Y, Thiyagarajan M, et al. Sleep drives metabolite clearance from the adult brain. Science. 2013;342(6156):373–77.
4. Carlstrom LP, Eltanahy A, Perry A, Rabinstein AA, Elder BD, Morris JM, et al. T.C.: a clinical primer for the glymphatic system. Brain. 2022;145(3):843–57.
5. Liu H, Chen L, Zhang C, Liu C, Li Y, Cheng L, Ouyang Y, Rutledge C, Anderson J, Wei Z, et al. Glymphatic influx and clearance are perturbed in huntington's disease. JCI Insight. 2024;9(20):172286.
6. Nedergaard M, Goldman, S.A. Glymphatic failure as a final common pathway to dementia. Science. 2020;370(6512):50–56.
7. Wardlaw JM, Benveniste H, Nedergaard M, Zlokovic BV, Mestre H, Lee H, et al. Perivascular spaces in the brain: anatomy, physiology and pathology. Nat Rev Neurol. 2020;16(3):137–53.
8. Nepozitek J, Dusek P, Sonka K. Glymphatic system, sleep, and parkinson's disease–interconnections, research opportunities, and potential for disease modification. Sleep. 2024;251.
9. Bojarskaite L, Vallet A, Bjørnstad DM, Gullestad Binder KM, Cunen C, Heuser K, et al. Sleep cycle-dependent vascular dynamics in male mice and the predicted effects on perivascular cerebrospinal fluid flow and solute transport. Nat Commun. 2023;14(1):953.
10. Boster KA, Cai S, Ladrón-de-Guevara A, Sun J, Zheng X, Du T, et al. Artificial intelligence velocimetry reveals in vivo flow rates, pressure gradients, and shear stresses in murine perivascular flows. Proc Natl Acad Sci, India, Sect B Biol Sci. 2023;120(14):2217744120.
11. Miao A, Luo T, Hsieh B, Edge CJ, Gridley M, Wong RTC, et al. Brain clearance is reduced during sleep and anesthesia. Nat Neurosci. 2024.
12. Mestre H, Tithof J, Du T, Song W, Peng W, Sweeney AM, et al. Flow of cerebrospinal fluid is driven by arterial pulsations and is reduced in hypertension. Nat Commun. 2018;9(1):4878.
13. Raghunandan A, Ladron-de-Guevara A, Tithof J, Mestre H, Du T, Nedergaard M, et al. Bulk flow of cerebrospinal fluid observed in periarterial spaces is not an artifact of injection. Elife. 2021;10:65958.
14. Min Rivas F, Liu J, Martell BC, Du T, Mestre H, Nedergaard M, et al. Surface periarterial spaces of the mouse brain are open, not porous. J R Soc Interface. 2020;17(172):20200593.
15. Raicevic N, Forer JM, Ladrón-de-Guevara A, Du T, Nedergaard M, Kelley DH, et al. Sizes and shapes of perivascular spaces surrounding murine pial arteries. Fluids Barriers CNS. 2023;20(1):1–18.
16. Schain AJ, Melo-Carrillo A, Strassman AM, Burstein R. Cortical spreading depression closes paravascular space and impairs glymphatic flow: implications for migraine headache. J Neurosci. 2017;37(11):2904–15.
17. Boster KAS, Tithof J, Cook DD, Thomas JH, Kelley DH. Sensitivity analysis on a network model of glymphatic flow. J R Soc Interface. 2022;19(191):20220257.
18. Bedussi B, Almasian M, Vos J, VanBavel E, Bakker EN. Paravascular spaces at the brain surface: low resistance pathways for cerebrospinal fluid flow. J Cereb Blood Flow Metab. 2018;38(4):719–26.
19. Carr JB, Thomas JH, Liu J, Shang JK. Peristaltic pumping in thin nonaxisymmetric annular tubes. J Fluid Mech. 2021;917:10.
20. Gan Y, Holstein-Rønsbo S, Nedergaard M, Boster KA, Thomas JH, Kelley DH. Perivascular pumping of cerebrospinal fluid in the brain with a valve mechanism. J R Soc Interface. 2023;20(206):20230288.
21. Tithof J, Boster KA, Bork PA, Nedergaard M, Thomas JH, Kelley DH. A network model of glymphatic flow under different experimentally-motivated parametric scenarios. Iscience. 2022;25(5).
22. Tithof J, Kelley DH, Mestre H, Nedergaard M, Thomas JH. Hydraulic resistance of periarterial spaces in the brain. Fluids Barriers CNS. 2019;16:1–13.
23. Christensen J, Wright DK, Yamakawa GR, Shultz SR, Mychasiuk R. Repetitive mild traumatic brain injury alters glymphatic clearance rates in limbic structures of adolescent female rats. Sci Rep. 2020;10(1):6254.
24. Mortensen KN, Lilius T, Rosenholm M, Sigurðsson B, Kelley DH, Nedergaard M. Perivascular cerebrospinal fluid inflow matches interstitial fluid efflux in anesthetized rats. iScience. 2025;28(5).
25. Mortensen KN, Sanggaard S, Mestre H, Lee H, Kostrikov S, Xavier AL, et al. Impaired glymphatic transport in spontaneously hypertensive rats. J Neurosci. 2019;39(32):6365–77.
26. Kelley DH, Thomas JH. Cerebrospinal fluid flow. Annu Rev Fluid Mech. 2023;55:237–64.
27. Algin O, Cetinkaya K, Oto C, Ayberk G. Evaluation of the glymphatic system in rabbits using gadobutrol-enhanced mr cisternography with t1 and t2 mapping. NMR Biomed. 2025;38(2):5314.
28. Kameya N, Sakai I, Saito K, Hamabe-Horiike T, Shinmyo Y, Nakada M, et al. Evolutionary changes leading to efficient glymphatic circulation in the mammalian brain. Nat Commun. 2024;15(1):1–17.
29. Bohr T, Hjorth PG, Holst SC, Hrabětová S, Kiviniemi V, Lilius T, et al. The glymphatic system: current understanding and modeling. IScience. 2022;25(9).

30. Sangalli L, Boggero I. The impact of sleep components, quality and patterns on glymphatic system functioning in healthy adults: a systematic review. Sleep Med: X. 2023;101:322–49.
31. Chong PL, Garic D, Shen MD, Lundgaard I, Schwichtenberg AJ. Sleep, cerebrospinal fluid, and the glymphatic system: a systematic review. Sleep Med Rev. 2022;61:101572.
32. Fultz NE, Bonmassar G, Setsompop K, Stickgold RA, Rosen BR, Polimeni JR, et al. Coupled electrophysiological, hemodynamic, and cerebrospinal fluid oscillations in human sleep. Science. 2019;366(6465):628–31.
33. Lohela TJ, Lilius TO, Nedergaard M. The glymphatic system: implications for drugs for central nervous system diseases. Nat Rev Drug Discov. 2022;21(10):763–79.
34. Naganawa S, Taoka T. The glymphatic system: a review of the challenges in visualizing its structure and function with mr imaging. Magnetic Reson Med Sci. 2022;21(1):182–94.
35. Liu G, Ladrón-de-Guevara A, Izhiman Y, Nedergaard M, Du T. Measurements of cerebrospinal fluid production: a review of the limitations and advantages of current methodologies. Fluids Barriers CNS. 2022;19(1):101.
36. Rudick R, Zirretta D, Herndon R. Clearance of albumin from mouse subarachnoid space: a measure of csf bulk flow. J Neurosci Methods. 1982;6(3):253–59.
37. Pardridge WM. Csf, blood-brain barrier, and brain drug delivery. Expert Opin Drug Delivery. 2016;13(7):963–75.
38. Chiu C, Miller MC, Caralopoulos IN, Worden MS, Brinker T, Gordon ZN, et al. Temporal course of cerebrospinal fluid dynamics and amyloid accumulation in the aging rat brain from three to thirty months. Fluids Barriers CNS. 2012;9:1–8.
39. Davson H, Welch K, Segal MB. Physiology and pathophysiology of the cerebrospinal fluid. (No Title) (1987.
40. Masseguin C, LePanse S, Corman B, Verbavatz J, Gabrion J. Aging affects choroidal proteins involved in csf production in sprague-dawley rats. Neurobiol Aging. 2005;26(6):917–27.
41. Ushiki T, Takeda M. Three-dimensional ultrastructure of the perivascular space in the rat thymus. Arch Histol Cytol. 1997;60(1):89–99.
42. Ichimura T, Fraser P, Cserr HF. Distribution of extracellular tracers in perivascular spaces of the rat brain. Brain Res. 1991;545(1–2):103–13.
43. Kida S, Pantazis A, Weller R. Csf drains directly from the subarachnoid space into nasal lymphatics in the rat. anatomy, histology and immunological significance. Neuropathol Appl Neurobiol. 1993;19(6):480–88.
44. Sokołowski W, Barszcz K, Kupczyńska M, Czubaj N, Skibniewski M, Purzyc H. Lymphatic drainage of cerebrospinal fluid in mammals–are arachnoid granulations the main route of cerebrospinal fluid outflow? Biologia. 2018;73(6):563–68.
45. Johnston M, Zakharov A, Papaiconomou C, Salmasi G, Armstrong D. Evidence of connections between cerebrospinal fluid and nasal lymphatic vessels in humans, non-human primates and other mammalian species. Cerebrospinal Fluid Res. 2004;1(1):2.
46. Ma Q, Ineichen BV, Detmar M, Proulx ST. Outflow of cerebrospinal fluid is predominantly through lymphatic vessels and is reduced in aged mice. Nat Commun. 2017;8(1):1434.
47. Zhang E, Richards H, Kida S, Weller R. Directional and compartmentalised drainage of interstitial fluid and cerebrospinal fluid from the rat brain. Acta Neuropathologica. 1992;83:233–39.
48. Di Palma C, Goulay R, Chagnot S, Martinez De Lizarrondo S, Anfray A, Salaun J-P, et al. Cerebrospinal fluid flow increases from newborn to adult stages. Dev Neurobiol. 2018;78(9):851–58.
49. Iliff JJ, Lee H, Yu M, Feng T, Logan J, Nedergaard M, et al. Brain-wide pathway for waste clearance captured by contrast-enhanced mri. J Clin Investigation. 2013;123(3):1299–309.
50. Li L, Chopp M, Ding G, Davoodi-Bojd E, Zhang L, Li Q, et al. Mri detection of impairment of glymphatic function in rat after mild traumatic brain injury. Brain Res. 2020;1747:147062.
51. Hussain R, Tithof J, Wang W, Cheetham-West A, Song W, Peng W, et al. Potentiating glymphatic drainage minimizes post-traumatic cerebral oedema. Nature. 2023;1–9.
52. Lin L, Hao X, Li C, Sun C, Wang X, Yin L, et al. Impaired glymphatic system in secondary degeneration areas after ischemic stroke in rats. J Stroke CEREBROVASCULAR Dis. 2020;29(7):104828.
53. Gaberel T, Gakuba C, Goulay R, De Lizarrondo SM, Hanouz J-L, Emery E, et al. Impaired glymphatic perfusion after strokes revealed by contrast-enhanced mri: a new target for fibrinolysis? Stroke. 2014;45(10):3092–96.
54. Kim D, Gan Y, Nedergaard M, Kelley DH, Tithof J. Image analysis techniques for in vivo quantification of cerebrospinal fluid flow. Exp Fluids. 2023;64(11):181.
55. Benveniste H, Lee H, Ding F, Sun Q, Al-Bizri E, Makaryus R, et al. Anesthesia with dexmedetomidine and lowdose isoflurane increases solute transport via the glymphatic pathway in rat brain when compared with high-dose isoflurane. Anesthesiology. 2017;127(6):976–88.
56. Lilius TO, Blomqvist K, Hauglund NL, Liu G, Stæger FF, Bærentzen S, et al. Dexmedetomidine enhances glymphatic brain delivery of intrathecally administered drugs. J Control Release. 2019;304:29–38.
57. Schwartz D, Clark T. Affinity of detomidine, medetomidine and xylazine for alpha-2 adrenergic receptor subtypes. J Vet Pharmacol Ther. 1998;21(2):107–11.
58. Dittmar MS, Fehm NP, Vatankhah B, Horn M. Ketamine/Xylazine anesthesia for radiologic imaging of neurologically impaired rats: dose response, respiratory depression, and management of complications. Comp Med. 2004;54(6):652–55.
59. Hart CY, Burnett JC Jr, Redfield MM. Effects of avertin versus xylazineketamine anesthesia on cardiac function in normal mice. Am J Physiol-Heart Circulatory Physiol. 2001.
60. Kelley DH, Ouellette NT. Using particle tracking to measure flow instabilities in an undergraduate laboratory experiment. Am J Phys. 2011;79(3):267–73.
61. Ouellette NT, Xu H, Bodenschatz E. A quantitative study of three-dimensional lagrangian particle tracking algorithms. Exp Fluids. 2006;40:301–13.
62. Santisakultarm TP, Cornelius NR, Nishimura N, Schafer AI, Silver RT, Doerschuk PC, et al. In vivo two-photon excited fluorescence microscopy reveals cardiac-and respiration-dependent pulsatile blood flow in cortical blood vessels in mice. Am J Physiol-Heart Circulatory Physiol. 2012;302(7):1367–77.
63. Stefanovska A, Haken H, McClintock PV, Hožič M, Bajrović F, Ribarič S. Reversible transitions between synchronization states of the cardiorespiratory system. Phys Rev E Lett. 2000;85(22):4831.
64. Novo M, Freire S, Al-Soufi W. Critical aggregation concentration for the formation of early amyloid-ß (1–42) oligomers. Sci Rep. 2018;8(1):1783.
65. Gan Y, Thomas JH, Kelley DH. Gaps in the wall of a perivascular space act as valves to produce a directed flow of cerebrospinal fluid: a hoop-stress model. J R Soc Interface. 2024;21(213):20230659.
66. Julien C. The enigma of mayer waves: facts and models. Cardiovasc Res. 2006;70(1):12–21.
67. Bumstead JR, Bauer AQ, Wright PW, Culver JP. Cerebral functional connectivity and mayer waves in mice: phenomena and separability. J Cereb Blood Flow Metab. 2017;37(2):471–84.
68. Piao Y, Liu Y, Xie X. Change trends of organ weight background data in sprague dawley rats at different ages. J Toxicol Pathol. 2013;26(1):29–34.
69. Agrawal H, Davis J, Himwich W. Developmental changes in mouse brain: weight, water content and free amino acids. J Neurochem. 1968;15(9):917–23.
70. Liu G, Mestre H, Sweeney AM, Sun Q, Weikop P, Du T, et al. Direct measurement of cerebrospinal fluid production in mice. Cell Rep. 2020;33(12).
71. Guo Y, Quirk K, Kelley DH, Thomas JH. Advection and diffusion in perivascular and extracellular spaces in the brain. J R Soc Interface. 2025;22(226):20250010.
72. Holstein-Rønsbo S, Gan Y, Giannetto MJ, Rasmussen MK, Sigurdsson B, Beinlich FRM, et al. Glymphatic influx and clearance are accelerated by neurovascular coupling. Nat Neurosci. 2023;1–12.
73. Ambarki K, Baledent O, Kongolo G, Bouzerar R, Fall S, Meyer M-E. A new lumped-parameter model of cerebrospinal hydrodynamics during the cardiac cycle in healthy volunteers. IEEE Trans Biomed Eng. 2007;54(3):483–91.
74. Beggs CB. Cerebral venous outflow and cerebrospinal fluid dynamics. Veins Lymphatics. 2014;3(3.
75. Ringstad G, Eide PK. Cerebrospinal fluid tracer efflux to parasagittal dura in humans. Nat Commun. 2020;11(1):354.
76. Yoon J-H, Jin H, Kim HJ, Hong SP, Yang MJ, Ahn JH, et al. Nasopharyngeal lymphatic plexus is a hub for cerebrospinal fluid drainage. Nature. 2024;1–10.
77. Smyth LC, Xu D, Okar SV, Dykstra T, Rustenhoven J, Papadopoulos Z, et al. Identification of direct connections between the dura and the brain. Nature. 2024;1–9.
78. Gericke A, Martinka P, Nazarenko I, Persson PB, Patzak A. Impact of α1-adrenoceptor expression on contractile properties of vascular smooth muscle cells. Am J Physiol-Regul, Intgr Comp Physiol. 2007;293(3):1215–21.
79. Janssen BJ, De Celle T, Debets JJ, Brouns AE, Callahan MF, Smith TL. Effects of anesthetics on systemic hemodynamics in mice. Am J Physiol-Heart Circulatory Physiol. 2004;287(4):1618–24.
80. Sashindranath M, Sturgeon SA, French S, Craenmehr DD, Selan C, Freddi S, et al. The mode of anesthesia influences outcome in mouse models of arterial thrombosis. Res Pract Thromb Haemostasis. 2019;3(2):12184.

81. Kersten K, Visser KE, Miltenburg MH, Jonkers J. Genetically engineered mouse models in oncology research and cancer medicine. EMBO Mol Med. 2017;9(2):137–53.
82. Wong PC, Cai H, Borchelt DR, Price DL. Genetically engineered mouse models of neurodegenerative diseases. Nat Neurosci. 2002;5(7):633–39.
83. Dennis MB Jr. Humane endpoints for genetically engineered animal models. Ilar J. 2000;41(2):94–98.
84. Festing S, Wilkinson R. The ethics of animal research: talking point on the use of animals in scientific research. EMBO Rep. 2007;8(6):526–30.
85. Seymour RS, Hu Q, Snelling EP, White CR. Interspecific scaling of blood flow rates and arterial sizes in mammals. J Exp Biol. 2019;222(7):199554.
86. West GB, Brown JH, Enquist BJ. A general model for the origin of allometric scaling laws in biology. Science. 1997;276(5309):122–26.
87. Li L, Ding G, Zhang L, Davoodi-Bojd E, Chopp M, Li Q, et al. Aging-related alterations of glymphatic transport in rat: in vivo magnetic resonance imaging and kinetic study. Front Aging Neurosci. 2022;14:841798.
88. Taoka T, Naganawa S. Glymphatic imaging using mri. J Magnetic Reson Imag. 2020;51(1):11–24.
89. May C, Kaye J, Atack JR, Schapiro M, Friedland R, Rapoport S. Cerebrospinal fluid production is reduced in healthy aging. Neurology. 1990;40(3_part_1):500–500.
90. Cserr HF. Physiology of the choroid plexus. Physiol Rev. 1971;51(2):273–311.
91. Bèchet NB, Shanbhag NC, Lundgaard I. Glymphatic pathways in the gyrencephalic brain. J Cereb Blood Flow Metab. 2021;41(9):2264–79.
92. Herculano-Houzel S. The glia/neuron ratio: how it varies uniformly across brain structures and species and what that means for brain physiology and evolution. Glia. 2014;62(9):1377–91.

Publisher's Note